Quasi-1D Exciton Channels in Strain-Engineered 2D Materials

Florian Dirnberger, ^{1,*} Jonas D. Ziegler, ^{2,*} Paulo E. Faria Junior, ³ Rezlind Bushati, ^{1,4} Takashi Taniguchi, ⁵ Kenji Watanabe, ⁶ Jaroslav Fabian, ³ Dominique Bougeard, ² Alexey Chernikov, ^{2,7,†} and Vinod M. Menon ^{1,4,‡}

¹Department of Physics, City College of New York, New York, New York 10031, USA

²Department of Physics, University of Regensburg, 93040 Regensburg, Germany

³Institute for Theoretical Physics, University of Regensburg, 93040 Regensburg, Germany

⁴Department of Physics, The Graduate Center, City University of New York, New York, New York 10016, USA

⁵International Center for Materials Nanoarchitectonics,
National Institute for Materials Science, Tsukuba, Ibaraki 305-004, Japan

⁶Research Center for Functional Materials, National Institute for Materials Science, Tsukuba, Ibaraki 305-004, Japan

⁷Dresden Integrated Center for Applied Physics and Photonic Materials
(IAPP) and Würzburg-Dresden Cluster of Excellence ct.qmat,
Dresden University of Technology, Dresden, 01187, Germany
(Dated: August 9, 2021)

Strain engineering is a powerful tool in designing artificial platforms for high temperature excitonic quantum devices. Combining strong light-matter interaction with robust and mobile exciton quasiparticles, two-dimensional transition metal dichalcogenides (2D TMDCs) hold great promise in this endeavor. However, realizing complex excitonic architectures based on strain-induced electronic potentials alone has proven to be exceptionally difficult so far. Here, we demonstrate deterministic strain-engineering of both single-particle electronic bandstructure and excitonic many-particle interactions. We create quasi-one-dimensional (1D) transport channels to confine excitons and simultaneously enhance their mobility through locally suppressed exciton-phonon scattering. Using ultrafast, all-optical injection and time-resolved readout, we realize highly directional exciton flow with up to $100\,\%$ anisotropy both at cryogenic and room temperatures. The demonstrated fundamental modification of the exciton transport properties in a deterministically strained 2D material with effectively tunable dimensionality has broad implications for both basic solid-state science and emerging technologies.

INTRODUCTION

On-demand accessibility of excitonic quantum many-body phases promises a leap towards next generation quantum optoelectronics [1, 2]. The rich variety of excitonic many-body states, including insulators [3, 4], superfluids [5, 6] and condensates [7], electron-hole liquids [8, 9], as well as superconductive [10] and ferromagnetic phases [11], offers exceptional opportunities to implement concepts of Hubbard model and other quantum simulators [2, 12–16] searching for suitable material platforms. In the key challenge of artificially tailoring the properties of excitonic systems towards supporting such exotic phases, strain engineering has been established as one of the most powerful techniques at hand [1, 17–19]. Owing to reduced dielectric screening and strong Coulomb-correlations, two-dimensional transition metal dichalcogenides (2D TMDCs) are a highly promising platform for room temperature implementations of these concepts. Strikingly, their van der Waals (vdW) nature further allows complex nanoscale strain architectures to be readily implemented with essentially arbitrary geometry – a degree of freedom in the design of quantum simulators comparable to lithographically defined superconducting circuits [2]. Additionally, while most studies concentrated on funneling excitons [20–23] or free electrons [24] into localized potential minima, recent reports [25, 26] suggest promising perspectives to manipulate the mobility of excitons via strain tuning. This provides a strong motivation to build strain-induced quasi-1D potentials for mobile exciton quasiparticles in an otherwise fully 2D system.

In this work, we demonstrate deterministic strain engineering of excitonic many-particle interactions, allowing to significantly enhance localization of excitons in one direction and their mobility in another. Merging 1D semiconductor nanowires with WSe₂ monolayers into hybrid heterostructures, we create artificial strain-induced exciton transport channels in the 2D matrix. Remarkably, these are found to exhibit near 100% anisotropy in the exciton flow not only at cryogenic but, most importantly, also at room temperatures. The underlying changes in the local multi-valley bandstructure are shown to strongly impact both confinement and dynamical motion of excitons, leading to their enhanced mobility within the channel. Our approach introduces a highly tunable platform to modify the effective dimensionality of the exciton motion, while fully retaining strong Coulomb and light-matter interaction of the pristine 2D material.

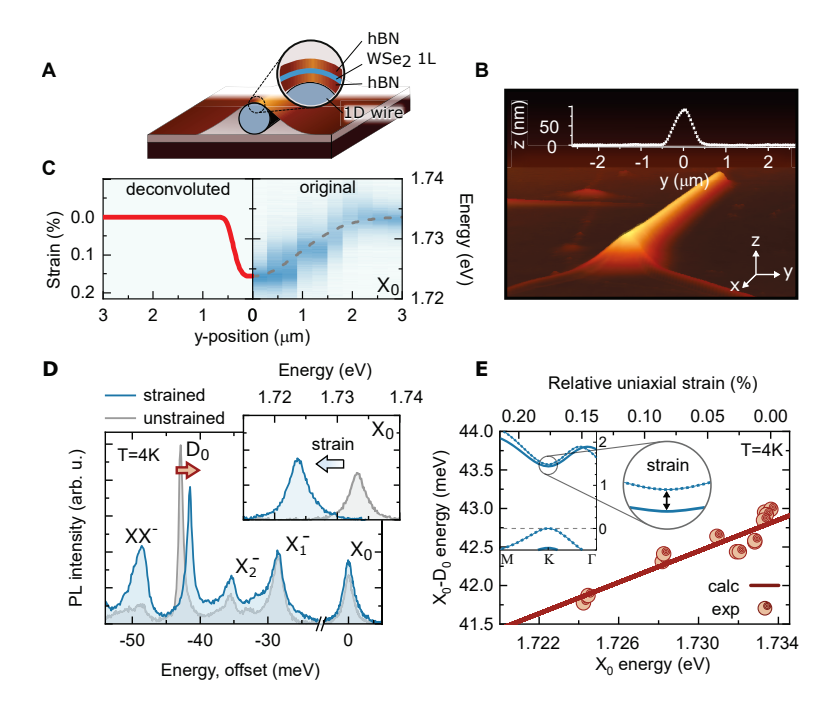


FIG. 1. Strain-engineered energy landscape in a hybrid 1D/2D structure. (A) Schematic illustration of the sample structure. (B) Topographic AFM image (inset: lateral height profile from the center). (C) Measured energy of the exciton emission of 1L WSe₂ in a false-color plot as a function of the spatial coordinate perpendicular to the nanowire direction. Shown are as-measured data (right) and a convolution of a super-Gaussian strain profile (left) with the optical collection spot (gray dashed line). (D) Extended μ -PL spectra of strained and unstrained regions as a function of the relative energy with respect to the X_0 resonance (inset: X_0 spectra plotted on absolute energy axis). (E) Measured and calculated energy splitting between bright (X_0) and spin-dark (X_0) excitons as a function of the X_0 peak energy (inset: first-principles electronic band structure of an unstrained 1L WSe₂, dashed and solid lines represent bands with different spin). Data in (C), (D) and (E) was obtained at X_0 and X_0 are X_0 and X_0 are X_0 and X_0 are X_0 and X_0 are X_0 and X_0 and X_0 are X_0 and X_0 and X_0 are X_0 and X_0 are X_0 are X_0 are X_0 are X_0 and X_0 are X_0 are X_0 are X_0 are X_0 and X_0 are X_0 are X_0 are X_0 are X_0 and X_0 are X_0 are X_0 and X_0 are X_0 are X_0 and X_0 are X_0 are X_0 are X_0 and X_0 are X_0 and X_0 are X_0 are X_0 and X_0 are X_0 are X_0 are X_0 and X_0 are X_0

RESULTS

Strain-engineered quasi-1D confinement potentials

Our hybrid 1D/2D structure is schematically illustrated in Fig. 1A. The active component which hosts excitons is a 1L WSe₂, fully encapsulated in high-quality hBN to provide uniform dielectric screening and suppress disorder. The hBN-WSe₂ stack is then placed on top of a GaAs/Al_{0.36}Ga_{0.64}As core/shell nanowire and is deformed to a 90 nm height over a length of about $8 \,\mu m$, as shown by the atomic force microscopy (AFM) image in Fig. 1B. This mechanical deformation with several 100 nm width leads to a pronounced spatial dependence of the spectral characteristics of 1L WSe₂. A series of micro-photoluminescence (μ -PL) scans, recorded along the transverse y-direction with respect to the nanowire axis at $T=4 \,\mathrm{K}$, is plotted both as-measured and deconvoluted by the optical resolution on the right and left sides of Fig. 1C, respectively. The data shows a pronounced shift of the extracted bright exciton resonance (X_0) as a function of the spatial coordinate y. Extended spectra are presented in Fig. 1D, plotted relative to the X_0 energy. Following the deformation, all detected emission features of 1L WSe₂, including dark states and higher-order complexes, shift accordingly (also see Supplementary Note 1).

Importantly, the absence of changes in the energy splitting between the exciton ground and excited states, as well as charged states detected in reflectance (see Supplementary Note 3), confirms uniform dielectric screening and doping in the structure. In particular, the high exciton binding energy of pristine hBN-encapsulated 1L WSe₂ on the order of 180 meV is kept unchanged across the channel.

From spectral analysis we thus unambiguously identify uniaxial strain induced by the nanowire in the mechanically deformed WSe₂ as the main cause for the local changes in the exciton energy landscape. The absence of additional spectral broadening of the X_0 emission peak observed in the center of the deformation in Fig. 1D indicates a largely uniform strain distribution within the μ -PL collection spot. To quantify the resulting potential from spectral observables, we use a super-Gaussian profile, also shown in Fig. 1C, which accurately approximates the spatially broadened X_0 energy profile after convolution with the optical collection spot. To determine strain we use a gauge factor from

first-principles calculations of $-63.2\,\mathrm{meV}$ per % strain for the absolute shift of the band gap. This scaling is largely consistent with reported room temperature values for 1L WSe₂ [25–27]. Therefore, we obtain a strain value of $0.15\,\%$, resulting in an attractive potential perpendicular to the nanowire direction with a depth on the order of $10\,\mathrm{meV}$. A detailed discussion of the strain profile analysis in our samples is provided in Supplementary Note S4.

Within the rich emission spectrum of 1L WSe₂, recent first-principles calculations predicted a subtle, yet uniquely characteristic fingerprint of strain – a shift between spin-allowed bright X_0 and spin-forbidden dark D_0 states [28, 29]. As apparent from Fig. 1E, we observe a continuous reduction of the X_0 - D_0 energy separation recorded in μ -PL scans across the deformation (cf. also Fig. 1D). It is consistent with the interpretation of strain determining the absolute shift of the exciton resonances in our samples. Quantitatively, the relative shift between X_0 and D_0 agrees with the value of $-6.4 \,\mathrm{meV}$ per % strain predicted from first-principle calculations (see Supplementary Note 2 and 4).

The resulting potential minimum enhances the local exciton density, as evidenced by the increase of charged biexciton emission (XX^-) in Fig. 1D) and, most importantly, strongly affects the exciton propagation (see Supplementary Note 5). All results presented in the manuscript were obtained from this device. Measurements conducted on several different devices on two separate hBN-encapsulated WSe₂ flakes confirm all main conclusions and are presented in the Supplementary Note S6.

Unidirectional exciton propagation at low temperature

We directly monitor the spatially resolved exciton dynamics through transient microscopy using pulsed optical excitation of the hybrid 1D/2D structure and detect the luminescence with a streak camera. Representative profiles of the exciton emission are presented in Fig. 2A and B along the direction parallel (x) and perpendicular (y) to the potential channel induced by the nanowire. Along the channel we observe characteristic spatial broadening of the emission over time from the expanding cloud of mobile excitons. In stark contrast to that, propagation perpendicular to the nanowire direction appears to be entirely suppressed.

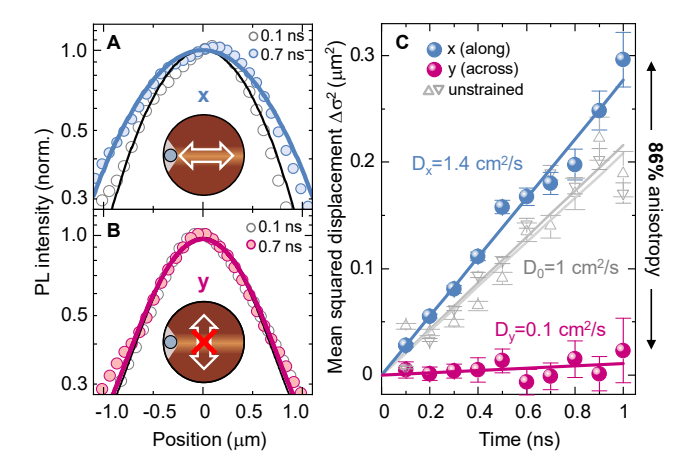


FIG. 2. Anisotropic exciton diffusion at T=4 K. (A) Spatially resolved exciton emission profiles obtained along the confinement channel direction (x), presented immediately after the excitation and at a later time of 0.7 ns. Gaussian fits are shown by solid lines. (B) Corresponding emission profiles measured across the channel (y). (C) Extracted time-dependent variance of the exciton distribution together with the data from the unstrained region. Error bars denote the standard error of the Gaussian fits at each time step. Corresponding diffusion coefficients from $\Delta\sigma(t)^2=2Dt$ and the resulting degree of anisotropy are indicated.

To quantify these observations, emission profiles at different times after the excitation are fitted with Gaussian functions, as illustrated in Fig. 2A and B. The resulting, time-dependent values of the variance, $\Delta\sigma(t)^2$, are presented in Fig. 2C for the two directions as well as in comparison to the measurements from an unstrained sample region. Along the confinement channel, $\Delta\sigma(t)^2$ increases linearly with time, characteristic for diffusive propagation. The diffusion coefficient $D_x = 1.4 \pm 0.1 \,\mathrm{cm}^2/\mathrm{s}$, extracted from the slope via $\Delta\sigma(t)^2 = 2Dt$, is comparable to the values in pristine, unstrained sample positions and is in reasonable agreement with low-temperature diffusion coefficients in hBN-encapsulated WSe₂ [30]. In contrast, the extracted effective diffusivity vanishes almost completely in the transverse direction, yielding $D_y = 0.1 \,\mathrm{cm}^2/\mathrm{s}$. The associated degree of anisotropy, $(D_x - D_y)/(D_x + D_y)$, is as high as 86%, emphasizing strongly directional exciton propagation along the strain-induced channel. Here, we note that

the determined anisotropy is fully reproducible across several devices and is very robust with respect to the excitation density (Supplementary Notes 6 and 8). Moreover, the PL in strained and unstrained regions of the monolayer exhibits very similar decay dynamics and can therefore not result in any anisotropy for the diffusion of excitons (see Supplementary Note 7).

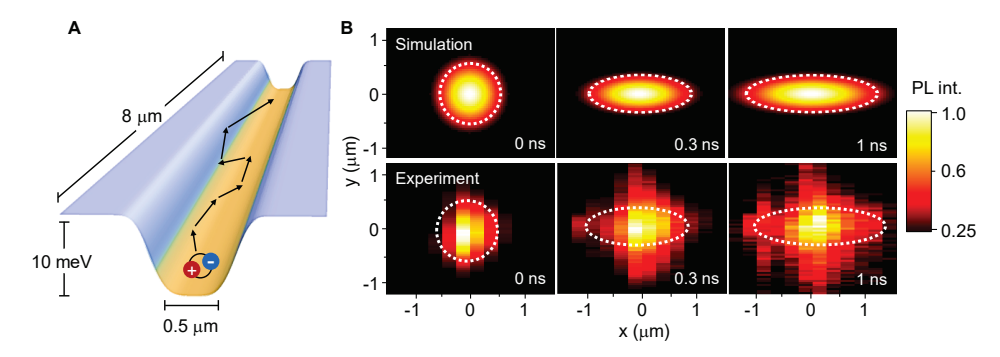


FIG. 3. Two-dimensional imaging of the transient exciton distribution at T=4 K. (A) Schematic illustration of the anisotropic diffusion along the quasi-1D channel. (B) Top: simulated images of the two-dimensional exciton density n(r,t) at different times after injection at the center of the potential well. Bottom: Corresponding experimentally obtained images of the exciton emission. Dashed lines are guides-to-the-eye.

It is interesting to consider that, particularly at very low temperatures, the confinement energy of $10 \,\mathrm{meV}$ should be fully sufficient to capture and constrain the excitons. In order to estimate the impact of such a strain potential, we simulate the exciton dynamics in our hybrid 1D/2D structure by constructing an attractive quasi-1D potential $u = u(\mathbf{r})$ based on the experimentally determined values for the strain profile and diffusion behavior from the unstrained area, as schematically illustrated in Fig. 3A. As excitons propagate diffusively inside the channel, even along y (see Supplementary Note 9), we characterize their motion by an isotropic diffusion coefficient D. A spatially- and time-resolved exciton density $n = n(\mathbf{r}, t)$ then evolves according to:

$$\frac{\partial n}{\partial t} = D\Delta n + \frac{D}{k_b T} (\nabla n \cdot \nabla u + n\Delta u) - \frac{n}{\tau}.$$
 (1)

The first term on the right-hand side accounts for diffusive free propagation, the second term arises from drift induced by the potential gradient, and the third term represents population decay (see Methods).

Simulated maps of the exciton density are presented in the upper panels of Fig. 3B, normalized at each time delay. The simulation clearly shows that the excitons injected from the 2D reservoir progressively adapt to the strain-induced confinement potential over time. While localized perpendicularly to the channel, the excitons are predicted to diffuse along the channel direction, supporting our observation of a highly anisotropic transport. For comparison, time-resolved 2D images of the measured emission are presented in the lower panels of Fig. 3B, obtained by manually scanning the detected segment of the image along the x-direction. The experiment shows the development of an increasingly elongated shape of the exciton emission over time after initially symmetric distribution.

Room temperature diffusion anisotropy

Following the discussion of highly anisotropic exciton transport at cryogenic temperatures, we now demonstrate that the observed high degree of propagation anisotropy is sustained even at room temperature. The measured time-dependent variance, $\Delta\sigma(t)^2$, of the exciton distribution is presented in Fig. 4A along and across the strain-induced channel at $T=290\,\mathrm{K}$. Similarly to our observations at $T=4\,\mathrm{K}$, we detect efficient diffusion along the nanowire direction with $D_x=13.5\pm1\,\mathrm{cm}^2/\mathrm{s}$ (corresponding to an effective mobility of $540\,\mathrm{cm}^2/\mathrm{Vs}$) and a diffusivity across the channel being close to zero. Interestingly, the latter even exhibits a small, negative value of $D_y=-0.8\pm0.1\,\mathrm{cm}^2/\mathrm{s}$, attributed to the shrinking of the exciton distribution. The possible impact of exciton funneling is further discussed in Supplementary Note 5. We note, that measurements on a second nanowire-induced deformation confirm the strong dependence on the direction of the exciton transport, while showing a diffusion of $D_y=0\,\mathrm{cm}^2/\mathrm{s}$ across the strain potential (see Supplementary Note 4). Experimentally, we thus effectively observe 100 % anisotropy in the exciton propagation.

Interestingly, considering the average thermal energy of the excitons on the order of 25 meV, the confinement potential alone should not lead to such a strong difference in effective diffusion coefficients (Supplementary Note 10).

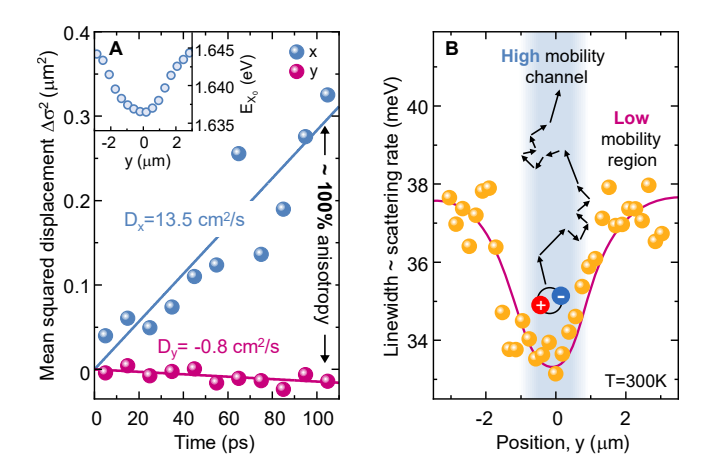


FIG. 4. Room temperature anisotropy in the exciton propagation (A) Time-dependent variance of the exciton distribution along (x) and across (y) the strain-induced channel at $T=290\,\mathrm{K}$. Inset: exciton emission energy as function of the y-coordinate. (B) Spectral linewidth of the exciton resonance corresponding to a spatially dependent scattering rate at room temperature. Data points are extracted from individual PL spectra recorded along y. The background schematically illustrates exciton propagation in a channel with comparatively weak scattering (high mobility) surrounded by regions of efficient scattering (low mobility). The blue shaded region approximates the width of the channel based on the underlying strain profile.

Here, a crucial feature of our hybrid 1D/2D platform comes into play: The excitons not only experience a spatially dependent change in their total energy, but also in their momentum scattering rate. As our measurements presented in Fig. 4B show for bright excitons, in agreement with recent reports [25, 26, 31, 32], a reduction of intervalley exciton-phonon scattering and the associated increase in exciton coherence occurs under strain due to substantial energy shifts across the multi-valley band structure. This leads to the very peculiar scenario, schematically illustrated in Fig. 4B – an emergence of a channel with suppressed scattering, favoring exciton propagation. This channel is surrounded by unstrained 1L WSe₂ with effectively lower mobility (also see Supplementary Note 10). This unique combination of strain-dependent scattering and coherence with an external confinement potential ultimately results in a highly anisotropic exciton transport at room temperature.

DISCUSSION

The demonstrated capability to deterministically guide neutral light-emitting quasiparticles along pre-defined pathways up to room temperature provides a particularly promising platform for the design of excitonic architectures and networks. Most importantly, the hybrid 1D/2D strain-based approach fully preserves the benefits of strong light-matter interactions and highly stable excitons of the 2D TMDC. Our platform should thus be highly attractive for controlling excitons in a broad variety of other novel low-dimensional structures, including vdW heterostructures designed to host interlayer [33] or Moiré-like excitations [34]. While strain-induced mobility enhancement and highly directional exciton transport with near 100 % anisotropy at room-temperature promises compelling advantages for exciton-based applications at ambient conditions, one can also anticipate fascinating low-temperature physics for channel widths smaller than about 60 nm (see Supplementary Note 9). Such strain-induced hybrid channels – highly promising to reach truly 1D regimes – may pave the way towards mesoscopic quantum transport phenomena of correlated many-body states, merging continuously tunable dimensionality with novel quasiparticle physics [35].

MATERIALS AND METHODS

Sample fabrication

The hybrid 1D-2D devices illustrated in Fig. 1A were assembled in a layer-by-layer bottom-up approach. First, standard SiO_2/Si substrates (oxide thickness $285\,\mathrm{nm}$) were cleaned using a high intensity ultrasonic bath in acetone and propan-2-ol for 2 min each and a subsequent blow dry using N_2 . In order to remove remaining adsorbates, the

samples underwent a O_2 plasma cleaning for 5 minutes at 200 W. Epitaxially grown $GaAs/Al_{0.36}Ga_{0.64}As$ core/shell nanowires, with (80 ± 9) nm diameter and a length of (8 ± 1) µm, were then deposited by bringing the as-grown nanowire wafer into mechanical contact with a clean SiO_2/Si substrate [36].

Several hBN-encapsulated WSe₂ heterostructures were fabricated as follows: hBN crystals supplied by colleagues from NIMS were cleaved and thinned down using two sheets of "Scotch Magic Tape". One of the tapes was then placed on polydimethylsiloxan (PDMS, WF-20-X4, Gel-Pak) without adding additional pressure. A suitable, few-nm thin hBN layer was chosen by its optical contrast and then stamped on top of several nanowires using a home-built sample holder heated to 100 °C. A single layer of WSe₂ was similarly exfoliated on PDMS from bulk crystals (acquired from HQgraphene) using blue tape (PVC tape 224PR, Nitto). The WSe₂ flake was stamped on top of the hBN at 70 °C, before a second layer of few-nm thin hBN was transferred on top at 70 °C [37]. The structure was annealed before every stamping step in a low-pressure forming gas atmosphere (10⁻² bar, 5% H₂ in N₂) at 150 °C for 2–4 h. Several tens of single nanowires were covered by the resulting van der Waals stack. We also note that the alternative method of drop casting nanowires from propan-2-ol solution instead resulted in a compromised optical quality of WSe₂ monolayers.

Optical spectroscopy

The sample was mounted inside a He-flow cryostat (KONTI Cryostat Type Microscope, CryoVac), placed on top of an inverted microscope (Eclipse Ti-U, Nikon) and held under high-vacuum conditions (10^{-8} bar) when measured at low temperatures. For time-integrated μ -PL mapping, we used continuous-wave laser excitation (LRS 0532 PFM, Laserglow technologies) at the photon energy of 2.33 eV and 0.4 μ W power. The laser beam was focused onto the sample to spot diameters of about $\sim 1.0 \,\mu$ m using either a $60 \times$ (CFI S Plan Fluor ELWD 60XC NA = 0.7, Nikon), or a $100 \times$ (TU Plan Fluor 100X NA = 0.9, Nikon) microscope objectives.

The resulting emission from the sample was filtered by a combination of two spectrally tunable filters with a spectrally sharp cut-off edge (VersaChrome Edge, Semrock) to remove both the laser light and the GaAs nanowire PL at $1.52\,\mathrm{eV}$, well below the band gap of the WSe₂ monolayer. A pinhole with 50 µm diameter was used to spatially filter the resulting PL from the excited region in the image plane before it was directed into a spectrometer (Acton SpectraPro SP-2300, Princeton Instruments) and dispersed onto a charged-coupled device (CCD) (Pixis 256, Princeton instruments). The full-width-at-half-maximum values in Fig. 4 were numerically determined from the spectrally resolved μ -PL line scan. For the linear reflectance spectroscopy measurements presented in Supplementary Note 3, we used the attenuated output of a spectrally broadband tungsten-halogen lamp (250W QTH, Newport) as a light source, spatially filtered and focused by the $60 \times$ microscope objective onto a spot size of $2.0\,\mu$ m. The reflected signal was detected by a CCD coupled to a spectrometer.

Time-resolved emission microscopy

For time-resolved emission microscopy measurements, 100 fs-pulses with 80 MHz repetition frequency from a tunable Ti:sapphire laser (Chameleon Ultra II, Coherent Inc.) set to operate at $1.77\,\mathrm{eV}$ were focused to a spot size of $1.0\,\mathrm{\mu m}$ using the $60\times(\mathrm{NA}=0.7)$ glas-corrected objective. To obtain the data in Figs. 2 and 3, an estimated electron-hole pair density of $\sim 10^{11}\,\mathrm{cm}^{-2}$ was injected by setting the excitation energy density to $5\,\mathrm{\mu J/cm^2}$ per pulse at $0.8\,\%$ absorption at the high-energy flank of the X_0 resonance (cf. also Supplementary Note 3). To minimize Auger-like exciton-exciton annihilation effects [38], room temperature experiments shown in Fig. 4 were performed at much smaller densities, using $0.5\,\mathrm{\mu J/cm^2}$ per pulse.

A lateral cross-section of the resulting PL emission was either directly imaged onto a streak camera (C10910, Hamamatsu) using a mirror for time- and spatially resolved measurements. For time- and spectrally resolved detection, a $300\,\mathrm{mm^{-1}}$ grating was used instead. In spatially resolved measurement the emission is measured either along (x) or across (y) the nanowire direction by rotating the sample relative to the detector slit. To obtain two-dimensional maps of the time-resolved emission in Fig. 3C, we align the sample in the y-direction parallel to the detector slit and subsequently image several cross-sections of the PL emission by manually shifting the image plane along the x-direction. These data are then combined to a two-dimensional image. For the analysis in Fig. 2 and Fig. 4, the emission profiles are integrated over $100\,\mathrm{ps}$ -time intervals and fitted by a Gaussian $(\sim \exp(-\mathbf{r}^2/\sigma(t)^2))$ to determine the transient change of the variance, $\Delta\sigma(t)^2 = \sigma(t)^2 - \sigma_0^2$, as a function of time. From $\Delta\sigma(t)^2 = 2Dt$ we obtain the diffusion coefficient D.

Numerical simulation of exciton transport

For numerical simulations, the time evolution of an initial Gaussian exciton density, $n(\mathbf{r},0) = n_0 \exp(-\mathbf{r}^2/2\sigma_0^2)$ with $\sigma_0 = 0.3 \,\mu\text{m}$, centered on top of the quasi-1D potential $u = u(\mathbf{r})$, was evaluated based on Eq. (1) using a spatial grid of 200x200 points with a step size of 0.04 μ m and a temporal resolution below 1 ps. As input, experimentally derived parameters, $D = 1.4 \, \text{cm}^2/\text{s}$, $\tau = 300 \, \text{ps}$ and a potential depth of 9 meV, were used. To compare the numerical results with the exciton emission profiles obtained in experiments, the calculated real-space distribution of excitons was convoluted with the point spread function of the objective lens approximated by a Gaussian with a full width at half maximum of $\sim 550 \, \text{nm}$. Including a position-dependent diffusion coefficient along the y-direction in Eq. (1) modifies the drift-diffusion model to account for a strain-dependent diffusivity emerging at elevated temperatures (cf. Supplementary Note 10).

First principles calculations of strained WSe2

The first-principles calculations were performed using density functional theory within the WIEN2k [39] software implementation. For the in-plane strain applied to the WSe₂ monolayer, the atomic positions were fully relaxed along the out-of-plane direction. A vacuum region of 20Å was considered to avoid the interaction between monolayer replicas. The self-consistent calculations were performed using a Monkhorst-Pack grid with 15×15 k-points, a corevalence energy separation of -6 Ry, a plane-wave cut-off multiplied by the smallest atomic radii of 9 and a convergence criteria of 10^{-6} e for the charge, 10^{-6} Ry for the energy and 10^{-1} mRy/bohr for the forces. Spin-orbit coupling was included fully relativistically for core electrons and via a second variational approach for valence electrons [40]. We systematically analyze the influence of different exchange-correlation functionals as well as the effect of biaxial and uniaxial strain. To estimate the number of excitonic levels confined in the strained region, we evaluate the Hamiltonian of the exciton center-of-mass subjected to an external confinement potential. Further details are discussed in Supplementary Note 2 and 9.

- * These authors contributed equally.
- † alexev.chernikov@tu-dresden.de
- [‡] menon@ccny.cuny.edu
- [1] Basov, D., Averitt, R. & Hsieh, D. Towards properties on demand in quantum materials. *Nature materials* **16**, 1077–1088 (2017).
- [2] Altman, E. et al. Quantum simulators: Architectures and opportunities. PRX Quantum 2, 017003 (2021).
- [3] Mazza, G. et al. Nature of symmetry breaking at the excitonic insulator transition: Ta 2 nise 5. Physical Review Letters 124, 197601 (2020).
- [4] Ma, L. et al. Strongly correlated excitonic insulator in atomic double layers. arXiv preprint arXiv:2104.05066 (2021).
- [5] Fogler, M., Butov, L. & Novoselov, K. High-temperature superfluidity with indirect excitons in van der waals heterostructures. *Nature communications* 5, 1–5 (2014).
- [6] Gupta, S., Kutana, A. & Yakobson, B. I. Heterobilayers of 2d materials as a platform for excitonic superfluidity. *Nature communications* 11, 1–7 (2020).
- [7] Wang, Z. et al. Evidence of high-temperature exciton condensation in two-dimensional atomic double layers. Nature 574, 76–80 (2019).
- [8] Keldysh, L. The electron-hole liquid in semiconductors. Contemporary physics 27, 395–428 (1986).
- [9] Arp, T. B., Pleskot, D., Aji, V. & Gabor, N. M. Electron–hole liquid in a van der waals heterostructure photocell at room temperature. *Nature Photonics* 13, 245–250 (2019).
- [10] Cotlet, O., Zeytinoğlu, S., Sigrist, M., Demler, E. & Imamoğlu, A. Superconductivity and other collective phenomena in a hybrid bose-fermi mixture formed by a polariton condensate and an electron system in two dimensions. *Physical Review B* 93, 054510 (2016).
- [11] Zhitomirsky, M., Rice, T. & Anisimov, V. Ferromagnetism in the hexaborides. Nature 402, 251–253 (1999).
- [12] Georgescu, I. M., Ashhab, S. & Nori, F. Quantum simulation. Reviews of Modern Physics 86, 153 (2014).
- [13] Tarruell, L. & Sanchez-Palencia, L. Quantum simulation of the hubbard model with ultracold fermions in optical lattices. Comptes Rendus Physique 19, 365–393 (2018).
- 14] Lagoudakis, P. G. & Berloff, N. G. A polariton graph simulator. New Journal of Physics 19, 125008 (2017).
- [15] Berloff, N. G. et al. Realizing the classical xy hamiltonian in polariton simulators. Nature materials 16, 1120–1126 (2017).
- [16] Kennes, D. M. et al. Moiré heterostructures as a condensed-matter quantum simulator. Nature Physics 1–9 (2021).
- [17] Butov, L., Lai, C., Ivanov, A., Gossard, A. & Chemla, D. Towards bose–einstein condensation of excitons in potential traps. *Nature* 417, 47–52 (2002).

- [18] Yoshioka, K., Chae, E. & Kuwata-Gonokami, M. Transition to a bose-einstein condensate and relaxation explosion of excitons at sub-kelvin temperatures. *Nature communications* **2**, 1–5 (2011).
- [19] Zhang, J. et al. Cooperative photoinduced metastable phase control in strained manganite films. Nature materials 15, 956–960 (2016).
- [20] Castellanos-Gomez, A. et al. Local strain engineering in atomically thin mos2. Nano letters 13, 5361-5366 (2013).
- [21] Branny, A., Kumar, S., Proux, R. & Gerardot, B. D. Deterministic strain-induced arrays of quantum emitters in a two-dimensional semiconductor. *Nature communications* 8, 1–7 (2017).
- [22] Cordovilla Leon, D. F., Li, Z., Jang, S. W., Cheng, C.-H. & Deotare, P. B. Exciton transport in strained monolayer wse2. Applied Physics Letters 113, 252101 (2018).
- [23] Moon, H. et al. Dynamic exciton funneling by local strain control in a monolayer semiconductor. Nano Letters 20, 6791–6797 (2020).
- [24] Harats, M. G., Kirchhof, J. N., Qiao, M., Greben, K. & Bolotin, K. I. Dynamics and efficient conversion of excitons to trions in non-uniformly strained monolayer ws2. *Nature Photonics* 14, 324–329 (2020).
- [25] Aslan, O. B., Deng, M. & Heinz, T. F. Strain tuning of excitons in monolayer wse2. Physical Review B 98, 115308 (2018).
- [26] Niehues, I. et al. Strain control of exciton-phonon coupling in atomically thin semiconductors. Nano letters 18, 1751–1757 (2018).
- [27] Carrascoso, F., Li, H., Frisenda, R. & Castellanos-Gomez, A. Strain engineering in single-, bi-and tri-layer mos2, mose2, ws2 and wse2. Nano Research 14, 1698–1703 (2021).
- [28] Zollner, K., Faria Junior, P. E. & Fabian, J. Strain-tunable orbital, spin-orbit, and optical properties of monolayer transition-metal dichalcogenides. *Physical Review B* **100**, 195126 (2019).
- [29] Feierabend, M., Khatibi, Z., Berghäuser, G. & Malic, E. Dark exciton based strain sensing in tungsten-based transition metal dichalcogenides. *Physical Review B* 99, 195454 (2019).
- [30] Wagner, K. et al. Nonclassical exciton diffusion in monolayer wse2. arXiv preprint arXiv:2107.11168 (2021).
- [31] Khatibi, Z. et al. Impact of strain on the excitonic linewidth in transition metal dichalcogenides. 2D Materials 6, 015015 (2018).
- [32] Rosati, R. et al. Strain-dependent exciton diffusion in transition metal dichalcogenides. 2D Materials 8, 015030 (2020).
- [33] Ross, J. S. et al. Interlayer exciton optoelectronics in a 2d heterostructure p-n junction. Nano letters 17, 638-643 (2017).
- [34] Bai, Y. et al. Excitons in strain-induced one-dimensional moiré potentials at transition metal dichalcogenide heterojunctions. Nature Materials 19, 1068–1073 (2020).
- [35] Deshpande, V. V., Bockrath, M., Glazman, L. I. & Yacoby, A. Electron liquids and solids in one dimension. Nature 464, 209–216 (2010).
- [36] Dirnberger, F. et al. Tuning spontaneous emission through waveguide cavity effects in semiconductor nanowires. Nano letters 19, 7287–7292 (2019).
- [37] Castellanos-Gomez, A. et al. Deterministic transfer of two-dimensional materials by all-dry viscoelastic stamping. 2D Materials 1, 011002 (2014).
- [38] Zipfel, J. et al. Exciton diffusion in monolayer semiconductors with suppressed disorder. Physical Review B 101, 115430 (2020).
- [39] Blaha, P. et al. Wien2k: An apw+lo program for calculating the properties of solids. The Journal of chemical physics 152, 074101 (2020).
- [40] Singh, D. J. & Nordstrom, L. *Planewaves, Pseudopotentials, and the LAPW method* (Springer Science & Business Media, 2006).
- [41] Li, Z. et al. Emerging photoluminescence from the dark-exciton phonon replica in monolayer wse 2. Nature communications 10, 1–7 (2019).
- [42] Liu, E. et al. Gate tunable dark trions in monolayer wse 2. Physical review letters 123, 027401 (2019).
- [43] Li, Z. et al. Direct observation of gate-tunable dark trions in monolayer wse2. Nano letters 19, 6886–6893 (2019).
- [44] He, M. et al. Valley phonons and exciton complexes in a monolayer semiconductor. Nature communications 11, 1–7 (2020).
- [45] Schmidt, R. et al. Reversible uniaxial strain tuning in atomically thin wse2. 2D Materials 3, 021011 (2016).
- [46] Niehues, I. et al. Strain tuning of the stokes shift in atomically thin semiconductors. Nanoscale 12, 20786–20796 (2020).
- [47] Zollner, K., Junior, P. E. F. & Fabian, J. Strain-tunable orbital, spin-orbit, and optical properties of monolayer transition-metal dichalcogenides. Phys. Rev. B 100, 195126 (2019).
- [48] Frisenda, R. et al. Biaxial strain tuning of the optical properties of single-layer transition metal dichalcogenides. npj 2D Materials and Applications 1, 1–7 (2017).
- [49] Kohn, W. & Sham, L. J. Self-consistent equations including exchange and correlation effects. Physical review 140, A1133 (1965).
- [50] Perdew, J. P. & Wang, Y. Accurate and simple analytic representation of the electron-gas correlation energy. Phys. Rev. B 45, 13244–13249 (1992).
- [51] Perdew, J. P., Burke, K. & Ernzerhof, M. Generalized gradient approximation made simple. Phys. Rev. Lett. 77, 3865–3868 (1996).
- [52] Perdew, J. P. et al. Restoring the density-gradient expansion for exchange in solids and surfaces. Phys. Rev. Lett. 100, 136406 (2008).
- [53] Duerloo, K.-A. N., Ong, M. T. & Reed, E. J. Intrinsic piezoelectricity in two-dimensional materials. The Journal of Physical Chemistry Letters 3, 2871–2876 (2012).
- [54] Kormányos, A. et al. k· p theory for two-dimensional transition metal dichalcogenide semiconductors. 2D Materials 2, 022001 (2015).

- [55] Byrnes, S. J. Multilayer optical calculations. arXiv preprint arXiv:1603.02720 (2016).
- [56] Raja, A. et al. Dielectric disorder in two-dimensional materials. Nature Nanotechnology 14, 832–837 (2019).
- [57] Stier, A. V. et al. Magnetooptics of exciton rydberg states in a monolayer semiconductor. Phys. Rev. Lett. 120, 057405 (2018).
- [58] Wagner, K. et al. Autoionization and dressing of excited excitons by free carriers in monolayer wse 2. Physical Review Letters 125, 267401 (2020).
- [59] Feierabend, M., Morlet, A., Berghäuser, G. & Malic, E. Impact of strain on the optical fingerprint of monolayer transitionmetal dichalcogenides. *Physical Review B* 96, 045425 (2017).
- [60] Leon, D. F. C., Li, Z., Jang, S. W. & Deotare, P. B. Hot exciton transport in ws e 2 monolayers. Physical Review B 100, 241401 (2019).
- [61] Tran, K. et al. Evidence for moiré excitons in van der waals heterostructures. Nature 567, 71-75 (2019).
- [62] Ruiz-Tijerina, D. A., Soltero, I. & Mireles, F. Theory of moiré localized excitons in transition metal dichalcogenide heterobilayers. Phys. Rev. B 102, 195403 (2020).
- [63] Berkelbach, T. C., Hybertsen, M. S. & Reichman, D. R. Theory of neutral and charged excitons in monolayer transition metal dichalcogenides. Phys. Rev. B 88, 045318 (2013).
- [64] Stier, A. V., McCreary, K. M., Jonker, B. T., Kono, J. & Crooker, S. A. Exciton diamagnetic shifts and valley zeeman effects in monolayer ws 2 and mos 2 to 65 tesla. *Nature communications* 7, 1–8 (2016).
- [65] Goryca, M. et al. Revealing exciton masses and dielectric properties of monolayer semiconductors with high magnetic fields. Nature communications 10, 1–12 (2019).

ACKNOWLEDGMENTS

We thank Mikhail M. Glazov for interesting and helpful discussions and Imke Gronwald for support with the AFM measurements. Work at CUNY was supported through the NSF QII TAQS 1936276 (F.D.), NSF EPMD: 1906096 (R.B.) and the Army Research Office MURI grant: W911NF-17-1-0312 (V.M.M.). Work at the University of Regensburg was funded by the Deutsche Forschungsgemeinschaft (DFG, German Research Foundation) through Emmy Noether Initiative (CH1672/1, A.C.), SFB 1277 (projects B05 and B07, A.C. and D.B.), SPP 2244 (CH1672/4-1, A.C.) and SPP 2196 (CH1672/3-1, A.C.). The project was also funded by the DFG through Projektnummer 451072703 (F.D.). K. W. and T.T. acknowledge support from the Elemental Strategy Initiative, conducted by the MEXT, Japan, Grant Number JPMXP0112101001, JSPS KAKENHI Grant Numbers JP20H00354 and the CREST (JPMJCR15F3), JST.

AUTHOR CONTRIBUTIONS

F.D. and J.D.Z. conceived and realized the experimental idea with input from V.M.M. and A.C., as well as analyzed and interpreted the results. Simulations were performed by J.D.Z. with support from R.B.; P.E.F.J. and J.F. performed the first-principles calculations; K.W. and T.T. provided the hBN crystals; F.D. and D.B. synthesized the GaAs nanowires; J.D.Z. and F.D. prepared the 1D/2D structures. All authors contributed to the writing of the manuscript. A.C and V. M. M supervised the project.

COMPETING INTERESTS

The authors declare that they have no competing interests.

DATA AVAILABILITY

All data needed to evaluate the conclusions in the paper are present in the paper and/or the Supplementary Materials.

SUPPLEMENTARY INFORMATION: Quasi-1D Exciton Channels in Strain-Engineered 2D Materials

Florian Dirnberger, ^{1,*} Jonas D. Ziegler, ^{2,*} Paulo E. Faria Junior, ³ Rezlind Bushati, ^{1,4} Takashi Taniguchi, ⁵ Kenji Watanabe, ⁶ Jaroslav Fabian, ³ Dominique Bougeard, ² Alexey Chernikov, ^{2,7,†} and Vinod M. Menon^{1,4,‡}

¹Department of Physics, City College of New York, New York, New York 10031, USA

²Department of Physics, University of Regensburg, 93040 Regensburg, Germany

³Institute for Theoretical Physics, University of Regensburg, 93040 Regensburg, Germany

⁴Department of Physics, The Graduate Center, City University of New York, New York, New York 10016, USA

⁵International Center for Materials Nanoarchitectonics,

National Institute for Materials Science, Tsukuba, Ibaraki 305-004, Japan

⁶Research Center for Functional Materials, National Institute for Materials Science, Tsukuba, Ibaraki 305-004, Japan

⁷Dresden Integrated Center for Applied Physics and Photonic Materials

(IAPP) and Würzburg-Dresden Cluster of Excellence ct.qmat,

Dresden University of Technology, Dresden, 01187, Germany

CONTENTS

1. Low-temperature WSe_2 emission spectra under strain	2
2. First principles calculations of strained WSe_2	2
3. Role of dielectric screening and residual doping	4
4. Determination of the deformation-induced strain profile	5
5. Impact of localization and funneling on exciton diffusion	6
6. Reproducibility of the anisotropic exciton diffusion measurements	7
7. Low-temperature exciton dynamics	7
8. Density-dependent measurements	8
9. Estimated occupation of transverse exciton modes in strain-induced confinement channels	10
10. Anisotropic exciton transport and position-dependent scattering at room-temperature	11

1. LOW-TEMPERATURE WSe₂ EMISSION SPECTRA UNDER STRAIN

Under photo-excitation at low temperatures, excitonic interactions in the presence of a multi-valley band structure lead to a rich PL emission spectrum reported for high-quality encapsulated monolayers WSe₂⁴¹⁻⁴⁴. The hBN encapsulation in our hybrid 1D-2D vdW heterostructures therefore allows us to monitor the impact of local strain on the emission of bright excitons (X_0) , negatively charged trions $(X_1^-$ and $X_2^-)$, neutral dark excitons (D_0) , negatively charged bi-excitons (XX^-) , dark trions (D^-) , an unidentified peak (T_1) , and phonon-assisted emission from dark states $(P_1$ and $P_2)$ in energy and position resolved μ -PL scans. Analogous to the emission of bright X_0 excitons discussed in the main manuscript, all peaks show a position-dependent shift of the emission energy along the transverse y-direction (see Fig. S1A). A comparison between the two PL spectra from an unstrained (grey) and a strained (blue) region of our sample depicted in Fig. S1B demonstrates the peak shift towards lower energy. However, in the longitudinal x-direction of our device the PL emission energy varies only slowly, since the mechanical deformation in the vdW stack induced by the underlying semiconductor nanowire primarily creates uniaxial strain, as exemplary shown for bright X_0 excitons in Fig. S1C.

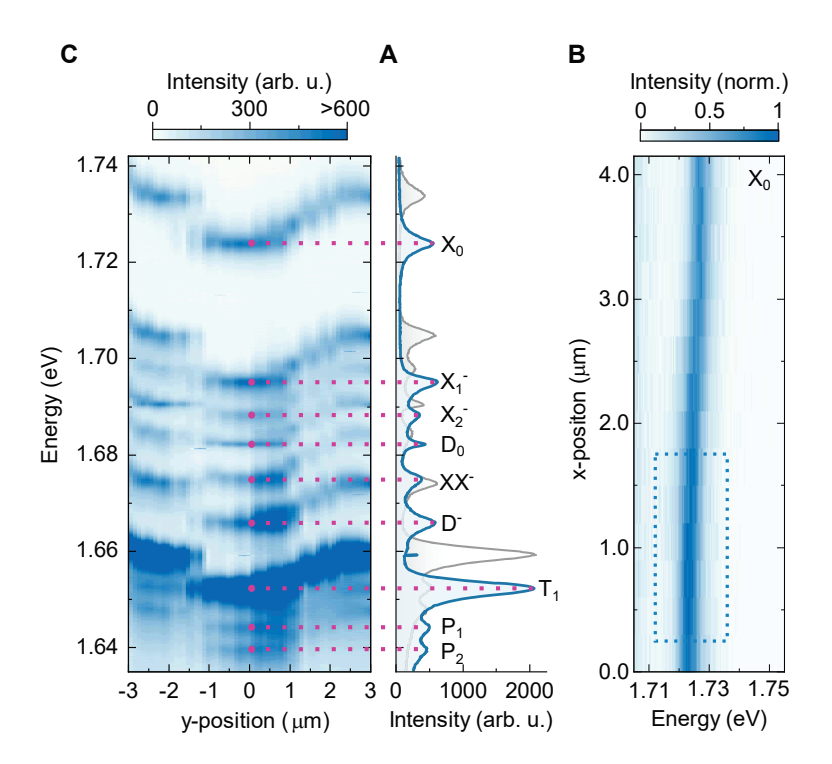
2. FIRST PRINCIPLES CALCULATIONS OF STRAINED WSe2

Recent studies have shown that experimentally observed excitonic transitions follow closely the strain dependence of the energy values calculated within the density functional theory (DFT) framework 45–47. The physical reason for such successful comparison of DFT and experiments is the following: although the single-particle energies experience strain effects more strongly, the effective masses and the dielectric screening are marginally affected. As a consequence, the exciton binding energy is almost independent of strain, especially in the presence of strong dielectric screening such as hBN encapsulation. Furthermore, strain calculations within the DFT framework remain consistent even when compared to more sophisticated theoretical approaches, for instance, that combine plain DFT to the effective Bethe-Salpeter equation (BSE)⁴⁷ or even full GW-BSE calculations⁴⁸.

Here, we investigate strained WSe₂ monolayers within DFT and analyze the impact of different exchange-correlation functionals, namely local density approximation (LDA)^{49,50}, Perdew–Burke-Ernzerhof (PBE)⁵¹ and PBEsol⁵². We also consider different orientations of strain since the relative alignment of the crystallographic axes of WSe₂ monolayer with respect to the nanowire axes is random in our samples.

In Fig. S2 we show the TMDC crystal structure and the unit cell for biaxial and uniaxial strain considered here. The in-plane lattice parameters are modified according to the type of strain applied. For biaxial strain,

$$a = (1 + \varepsilon) a_0, \tag{S1}$$



SUPPLEMENTARY FIGURE S1. Impact of local strain on the WSe₂ emission spectrum at low temperatures. (A) In the transverse y-direction, all peaks of the WSe₂ emission spectrum recorded in a μ -PL line scan shift to lower energy towards the center of the strain at y = 0. (B) Two exemplary PL spectra recorded in an unstrained sample position $(y = 3 \,\mu\text{m}, \text{grey})$ and a highly strained region in the center of the deformation $(y = 0 \,\mu\text{m}, \text{blue})$. (C) μ -PL line scan in the longitudinal x-direction mapping the X_0 emission along the mechanical deformation. The blue dashed rectangle marks the sample position used for the time-resolved diffusion experiments shown in the main manuscript. Scans in (A) and (C) were recorded under $40 \,\text{W/cm}^2$ and $400 \,\text{W/cm}^2$ power density of $2.33 \,\text{eV}$ continuous-wave excitation, respectively.

for uniaxial strain along x (armchair direction),

$$L_x = (1 + \varepsilon_{xx}) \sqrt{3} a_0$$

$$L_y = (1 - \nu \varepsilon_{xx}) a_0,$$
 (S2)

and for uniaxial strain along y (zigzag direction),

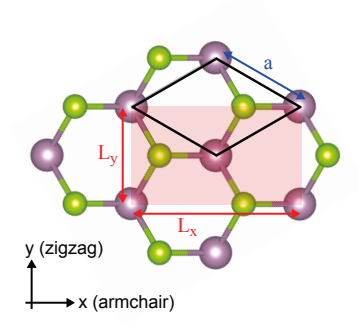
$$L_x = (1 - \nu \varepsilon_{yy}) \sqrt{3} a_0$$

$$L_y = (1 + \varepsilon_{yy}) a_0,$$
 (S3)

with ν being the Poisson ratio that accounts for the in-plane crystal deformation in the perpendicular in-plane direction of the applied strain. We consider $\nu = 0.1849$, taken from Ref.⁵³.

The optimized lattice parameters and the conduction band splittings (at the K valley) for unstrained WSe₂ obtained from our calculations are summarized in Table I. Relaxing the WSe₂ atomic structure with different exchange-correlation functionals provides slightly different optimized lattice parameters and consequently different conduction band splittings; however, the band alignment remains unchanged following the well know ordering in TMDCs⁵⁴.

The extracted gauge factors for the different functionals and strain types are summarized in Table II. Since biaxial strain acts on both directions simultaneously, we divide the obtained values by a factor of 2 in order to properly compare them with the uniaxial strain calculations. For uniaxial strain, we show the average gauge factor obtained for strain applied along the armchair and zigzag directions (they differ only at the first digit after the decimal). We emphasize that our calculation results consistently confirm the experimentally observed linear reduction of $X_0 - D_0$ under tensile strain, regardless of the choice of exchange-correlation functional and of the type of strain. As a



SUPPLEMENTARY FIGURE S2. Primitive unit cells for biaxial (solid black lines) and uniaxial (shaded rectangle) strain used in the calculations.

TABLE I. Optimised lattice parameters, a_0 and d_0 , and conduction band splittings at the K valley for the different exchange-correlation functionals considered in this study.

	LDA	PBE	PBEsol
a_0 (Å)	3.2485	3.3187	3.2706
d_0 (Å)	3.3343	3.3632	3.3516
$\Delta_{\rm CB}~({\rm meV})$	45.90	36.74	43.95

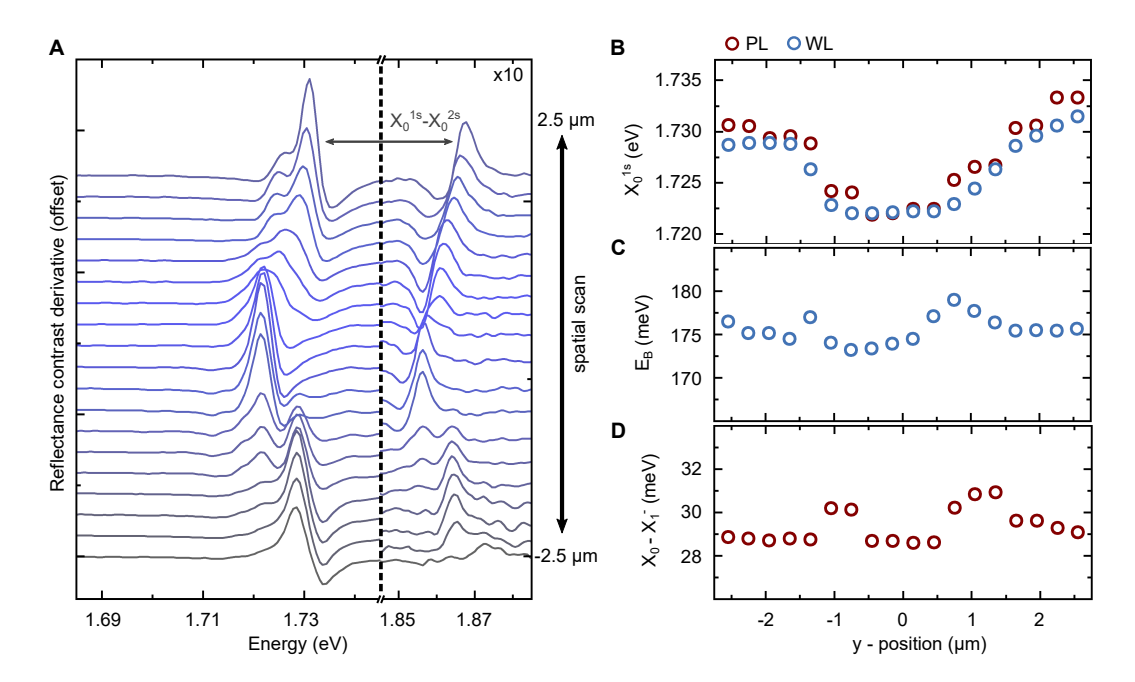
general trend, the individual gauge factors for X_0 and D_0 under uniaxial strain are smaller than the values for biaxial/2, whereas the $X_0 - D_0$ splitting is slightly larger.

3. ROLE OF DIELECTRIC SCREENING AND RESIDUAL DOPING

In order to exclude dielectric effects and to gain more insight into the role of background doping, we performed optical white light (WL) reflectance measurements using a spectrally broadband tungsten-halogen lamp in the same setup that we used for PL measurements. The reflectance contrast was calculated using $(R_{sample} - R_{ref})/(R_{ref} - R_{BG})$, where R_{sample} and R_{ref} spectra were acquired on the sample and in a reference position on the SiO₂/Si substrate in close proximity to the sample, respectively. Additionally, a background signal R_{BG} was acquired without the light source. Resonance energies and linewidths were extracted using a transfer-matrix formalism with model dielectric functions based on a series of Lorentz resonances^{55,56}. Exemplary reflectance contrast derivative spectra acquired at $T = 4 \,\mathrm{K}$ in a line-scan across the nanowire-induced deformation show the same strain-induced energy shift as the PL response (cf. Fig. S3A and B). The generally narrow linewidth of the reflectance resonances (less than 5 meV for both the strained and unstrained regions) highlights the absence of long-range disorder in the WSe₂ monolayer; only towards the edges of the strain-induced deformation, where the

TABLE II. Gauge factors (in meV/%) for X_0 , D_0 and $X_0 - D_0$ for the different exchange-correlation functionals and types of strain considered in this study.

	Gauge factors (meV/%)								
	LDA		PBE		PBEsol				
	Bi./2	Uni.	Bi./2	Uni.	Bi./2	Uni.			
X_0	-69.3	-63.2	-61.0	-54.4	-67.6	-59.8			
D_0	-64.9	-56.8	-58.0	-50.5	-63.4	-54.2			
$X_0 - D_0$	-4.4	-6.4	-3.0	-3.9	-4.2	-5.6			



SUPPLEMENTARY FIGURE S3. Impact of local strain on the reflectance contrast at $\mathbf{T} = 4 \, \mathbf{K}$. (A) Line scan across the nanowire-induced deformation in the y-direction with a step size of $0.3 \, \mu \mathrm{m}$. Reflectance spectra in the right part of the plot are multiplied by a factor of 10 to increase visibility. (B) Extracted energies of the ground state exciton resonance X_0^{1s} along the y-position (blue) in comparison to the X_0 PL emission determined from the line scan in Fig. 1C (red). (C) Exciton binding energy as a function of the y-position demonstrates a uniform dielectric screening across the hybrid 1D-2D structure. (D) Energy separation of the bright exciton (X_0) and first negatively charged trion (X_1^-) as function of the y-position from a PL line scan.

white light spot of about 2 µm collects signal from both unstrained and strained regions, we observe an additional broadening related to double peak features in the reflectance contrast.

The exciton binding energy E_B presented in Fig. S3C was estimated from the energy separation of the ground state and the first excited state by $E_B = 1.3(X_0^{1s} - X_0^{2s})$ according to the scaling for WSe₂ monolayers from Ref.⁵⁷. The resulting value of $E_B \approx 175 \,\mathrm{meV}$ is nearly constant across the hybrid 1D/2D device and merely small variations of a few meV arise at the edges of the strain-induced deformation due to the aforementioned broadening of the signal, demonstrating a homogeneous dielectric screening in our hybrid 1D/2D structures. Generally, a change in the binding energy due to a different dielectric environment is partially compensated by a renormalization of the free-particle band gap, resulting in a reduced energy shift of the ground state compared to the binding energy. In addition, since the spatial fluctuation of the binding energy shows no correlation with the energy shift of the X_0 peak, for which the maximum shift occurs in the center of the deformation, we exclude dielectric effects as reason for the position-dependent X_0 energy shift.

Moreover, reflectance measurements show no signatures of trion/Fermi polaron reflectance features in both strained and unstrained regions of our sample, which demonstrates an overall low level of residual doping and additionally excludes any significant contributions from strain-induced local doping effects. We estimate the doping level in our sample based on the energy separation between the bright X_0 exciton and the trion X_1^- peaks in PL: The comparison with a gate-tunable WSe₂ field-effect transistor device⁵⁸ determines an upper bound for the background electron density in our sample of $n_e = 5 \times 10^{11} \text{cm}^{-2}$. Furthermore, a nearly constant energy separation, $X_0 - X_1^-$, confirms the absence of local doping in the strained region (see Fig. S3D). Merely the edges of the strain-induced deformation show broadening-induced features similar to the reflectance measurements.

4. DETERMINATION OF THE DEFORMATION-INDUCED STRAIN PROFILE

Based on the results presented in the previous section, the position-dependent X_0 energy shift observed in μ -PL is a direct result of strain in our sample and can be used to estimate its magnitude and spatial distribution. We also emphasize that, in addition to the absolute shift of the X_0 energy, the relative shift between X_0 and D_0 exciton peaks (cf. Fig. 1E) in our experiments independently confirms the presence of tensile strain.

To derive the underlying strain profile from the spatially dependent X_0 energy shift, we need to account for the finite size of the μ -PL collection spot. As demonstrated in Fig. 1 of the main manuscript and in Fig. S1 of the Supplementary Information, the emission energy of X_0 excitons in our sample continuously decreases from 1.733 eV to 1.724 eV towards the point of maximum deformation, where it starts to increase again to the unstrained value, as expected for locally created strain. We note, that along the deformation created by the nanowire the X_0 energy, and therefore also the strain, remains nearly constant. In this analysis, the absence of any additional spectral broadening in the X_0 emission peak observed in the center of the deformation indicates a largely uniform strain distribution within the μ -PL collection spot. We therefore assume a Super-Gaussian strain profile, which is shown in Fig. 1C. This profile accurately describes the spatial broadening of the X_0 energy profile (dashed gray line in Fig. 1C-right panel) after convolution with a Gaussian to account for the finite resolution of the optical setup.

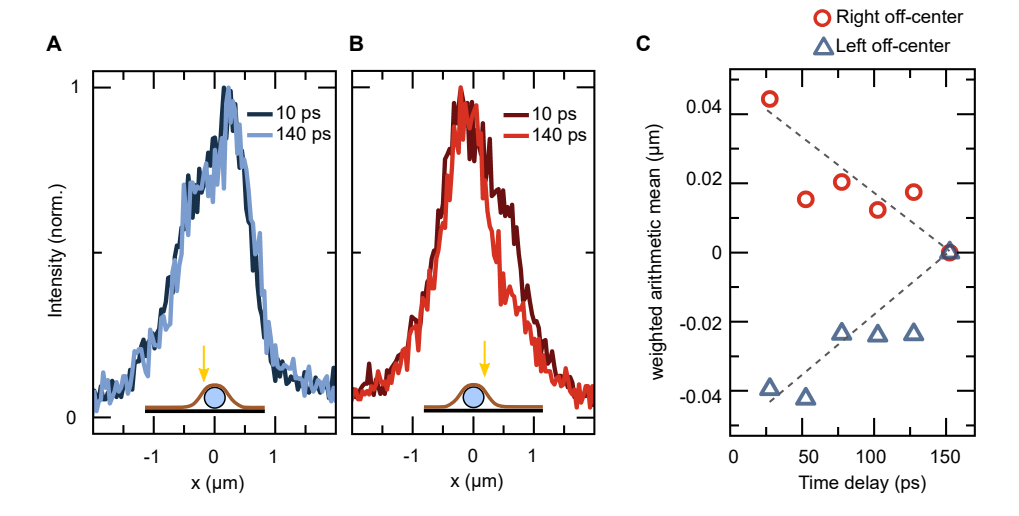
The magnitude of strain in our sample is estimated by calibrating the measured energy of the X_0 exciton peak to the change of the band gap energy obtained from first-principles DFT-LDA calculations (cf. Supplementary Note 2). Based on the calculated X_0 gauge factor of $-63.2\,\mathrm{meV/\%}$ strain, a line fitted to the experimental data points plotted in Fig. 1E determines a decrease of the X_0-D_0 separation by $-6.6\,\mathrm{meV/\%}$ strain, which excellently matches the corresponding calculated value of $-6.4\,\mathrm{meV/\%}$. For comparison, the same procedure based on first-principles DFT-PBEsol calculations, and thus a X_0 gauge factor of $-59.8\,\mathrm{meV/\%}$ strain, renders a decrease of the X_0-D_0 separation by $-6.3\,\mathrm{meV/\%}$, which still agrees reasonably well with the DFT-PBEsol calculated value of $-5.6\,\mathrm{meV/\%}$, but does not match the agreement with DFT-LDA calculations (cf. table in Supplementary Note 2). Hence, the DFT-LDA calculated gauge factor of $-63.2\,\mathrm{meV/\%}$ strain is used for X_0 throughout our study.

Previous experiments have reported comparable, albeit slightly lower scaling factors for X_0 (for example $-47.6 \,\mathrm{meV}/\%^{25}$, or $-49.0 \,\mathrm{meV}/\%^{26}$), while a recently published experimental study determined a gauge factor of $(-57 \pm 4) \,\mathrm{meV}/\%^{27}$ that is very close to the scaling that we use. We note, however, that all of the reported gauge factors listed above were determined at room temperature in contrast to the low-temperature conditions studied here. It is thus, for example, not obvious whether exciton-phonon coupling that contributes to temperature-dependent band gap renormalization could change under strain. To avoid potential uncertainties that may result as a consequence, it seems reasonable to use the calculated scaling factor until this point is clarified in future studies. Moreover, the resulting match of the relative energy separation between bright and dark exciton states in theory and experiment provides additional, strong support for our choice of the scaling.

5. IMPACT OF LOCALIZATION AND FUNNELING ON EXCITON DIFFUSION

In general, spatial variations in the exciton potential landscape are expected to induce drift currents which can funnel excitons along the gradients of the potential and result in their localization. However, there are also reports that challenge the role of exciton funneling in the description of strain-induced changes in the spatially dependent PL $^{20-24}$. Part of the apparent controversy in this regard might indeed relate to the different experimental realizations of the systems under study. More specifically, it appears crucial whether the samples exhibit a substantial amount of (dielectric) disorder inhibiting exciton movement, or whether the excitons can diffuse and drift more freely. Moreover, a careful spectral analysis of the detected resonance seems to be of particular importance. It thus seems likely that both experimental scenarios can exist: those in which funneling is present and those in which it will be largely suppressed.

In the following, we briefly discuss the potential role of exciton funneling in our experiments. In the hybrid 1D/2D systems, the length scale of the strain gradients relevant for exciton funneling is less than one micrometer, as determined by atomic force microscopy (see Fig. 1B and C of the main manuscript). Thus, directly resolving the exciton drift currents on such short length scales is difficult in optical diffusion measurements. Nevertheless, several observations in our experiments can be attributed to the occurrence of exciton funneling: when excitons are excited slightly off-center with respect to the strain-induced potential minimum, the resulting emission profiles show a small, transient shift of their center-of-mass towards the center of the deformation, as one would expect for the funneling of excitons. Figure S4A,B show normalized emission profiles at two different time delays for excitation on both sides of the 1D potential channel. The overall effect is small, yet the weighted arithmetic mean of the PL clearly shifts up to 50 nm towards the potential minimum (cf. Fig. S4C). The measurements are performed on both sides and the sign of the shift changes accordingly, supporting the interpretation of the observations as exciton funneling. In addition, we find strong indications of increased local density of the excitons that results in enhanced biexciton (XX^-) emission presented in Fig. 1C of the main manuscript. Finally, an overall higher PL intensity in the middle of the channel is consistent with funneling, even if it could also contribute to the observation of an effectively negative diffusion across the channel.



SUPPLEMENTARY FIGURE S4. Exciton diffusion measurements for excitation and collection at the side of the nanowire at T=4K. Normalized spatial PL profiles at early (10 ps) and later times (140 ps) after excitation on the left (A) and right (B) sides of the deformation. (C) Weighted arithmetic mean of the spatially resolved PL for the area -2 μm to 2 μm (shown in (A), (B)) shifts away from the excitation towards the middle for both sides of the strain-potential. Energy density per pulse was $5 \mu J/cm^2$ of pulsed excitation at $1.77 \, eV$. Dashed lines are guides to the eye.

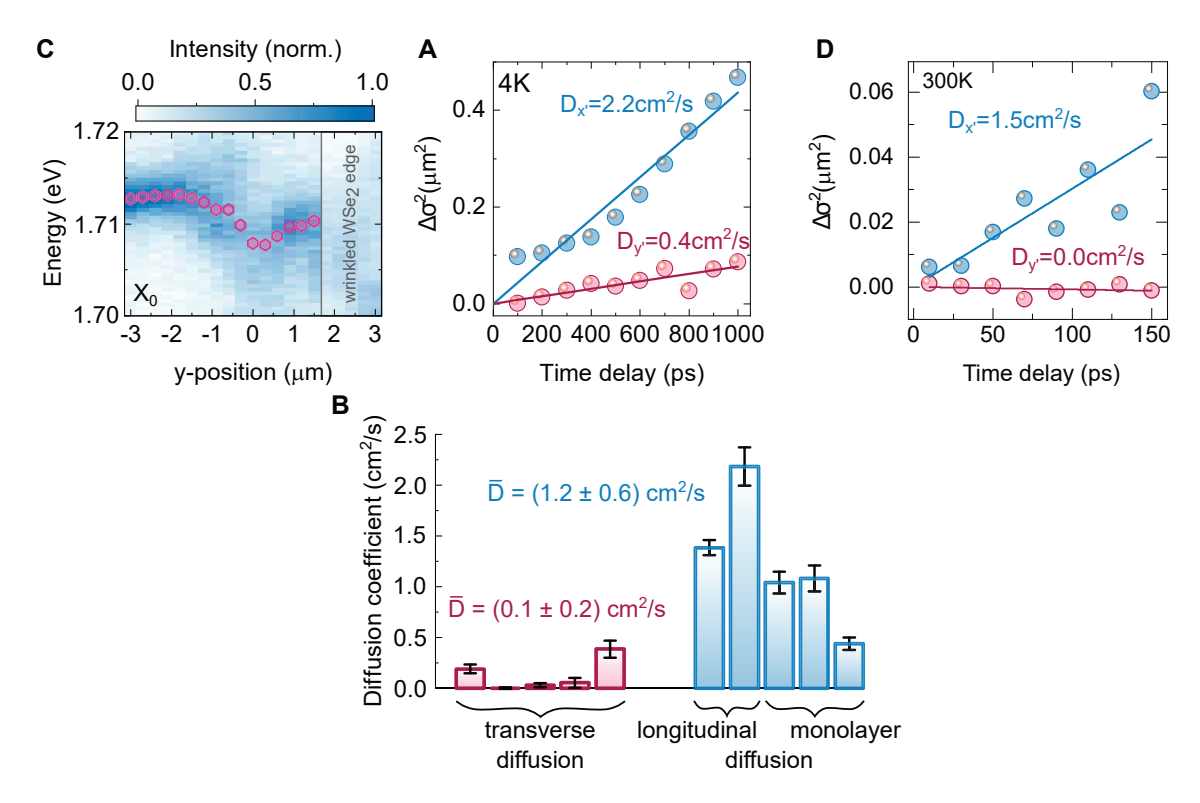
6. REPRODUCIBILITY OF THE ANISOTROPIC EXCITON DIFFUSION MEASUREMENTS

Supplementing the results obtained from the nanowire-induced deformation in the vdW stack discussed in the main manuscript, we observe similar phenomena in several studied 1D-2D structures. Figure S5A exemplary depicts the position-dependence of the X_0 emission peak for a different sample. Similar to the measurements presented in the main text, the X_0 peak shifts towards lower energy upon approaching the apex of the deformation in a μ -PL scan, reflecting the underlying strain-induced confinement potential. Correspondingly, time-resolved emission microscopy reveals a strongly anisotropic transport of excitons propagating along the longitudinal x'- and the transverse y'-direction of this hybrid 1D-2D structure (see Fig. S5B and C). Note that the value obtained in the transverse direction is likely to overestimate the diffusion coefficient since a certain contribution from the longitudinal component is expected due to a slight misalignment of the y'-axis relative to the detector slit in this particular measurement.

Additional hybrid 1D-2D devices, including nanowire-induced deformations in a second hBN/WSe₂ (1L)/hBN vdW stack, provide an average diffusion coefficient of $\overline{D}=1.2\,\mathrm{cm^2/s}$ for excitons propagating either along the longitudinal direction of a hybrid 1D-2D device, or within an unstrained monolayer at $T=4\,K$. In the transverse direction, we find an average value of $\overline{D}=0.1\,\mathrm{cm^2/s}$ in a number of different hybrid 1D-2D devices, as demonstrated in Fig. S5D. Hence, our analysis demonstrates a strongly anisotropic propagation of excitons in 1D-2D hybrid structures with an average anisotropy ratio exceeding one order of magnitude.

7. LOW-TEMPERATURE EXCITON DYNAMICS

Exciton decay dynamics can play an important role in determining diffusion coefficients in time-resolved emission microscopy measurements. As the collected PL signal is monitored in both time and space domains, diffusion coefficients derived from such a spectrally integrated measurement inherently reflect the average propagation of all detected species at low temperatures. In addition to that, spatial variations of the emission lifetime could potentially alter the apparent diffusion coefficient determined in these experiments. For example, if the deformation-induced strain would locally modify the exciton lifetime, as reported in a recent room-temperature study²⁶, different lifetimes would be expected in the center of the deformation (maximum strain) as compared to the lifetimes at the edges and far from the deformation (minimal strain). Such a scenario could potentially lead to an apparent change of the diffusion coefficient measured in the direction perpendicular to the channel. For the comparably small values of strain present in our hybrid 1D-2D structures, however, effects of strain on the exciton decay are not expected⁵⁹. Most importantly, a comparison of the decay dynamics in a strained and an unstrained region of our sample further shows that the lifetime of the excitons does not change significantly under strain in our experiment, as demonstrated in Fig. S6A. Hence, the exciton decay itself cannot result in any anisotropy of the exciton diffusion under strain.



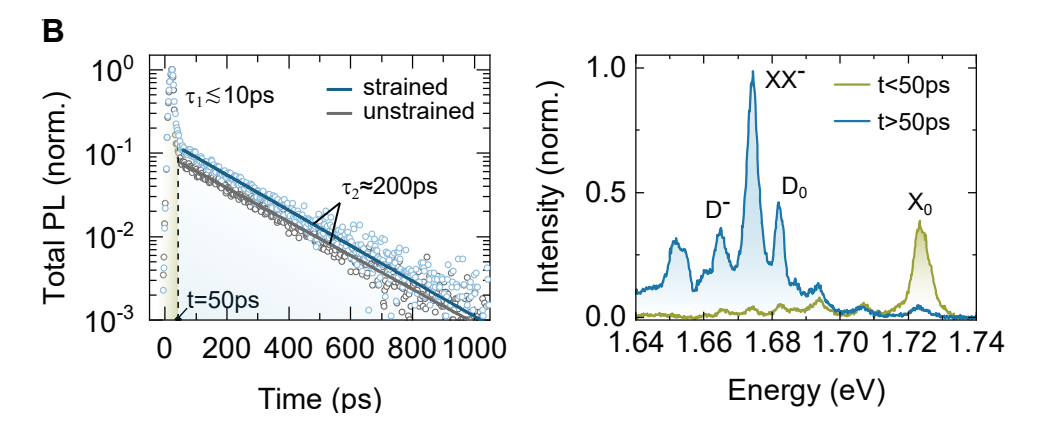
SUPPLEMENTARY FIGURE S5. Anisotropic exciton transport in additional devices. (A) μ -PL line scan showing the shift of the X_0 peak at $4\,K$ for a second hybrid 1D-2D device obtained under $400\,\mathrm{W/cm^2}$ power density and continuous-wave excitation with a photon energy of 2.33 eV. Pink circles indicate the peak energies determined from Gaussian fits. (B) and (C) Relative mean squared displacement from the spatially resolved exciton emission profiles, monitored at $4\,\mathrm{K}$ and $290\,\mathrm{K}$ in the longitudinal x'- and transverse y'-direction, respectively. These observations are characteristic for strongly anisotropic exciton transport. The energy density per pulse was set to $5\,\mathrm{\mu J/cm^2}$ and the photon energy to $1.77\,\mathrm{eV}$. (D) Summary of the measured diffusion coefficients at $4\,\mathrm{K}$. Values in brackets denote the average diffusion coefficient and its standard deviation, respectively.

In our experiments, the decay of the spectrally and spatially integrated total emission shows two regimes (see Fig. S3A): Initially, short-lived excitations dominate the PL signal (regime I, for $t < 50 \,\mathrm{ps}$), which is subsequently characterized by a much slower, single exponential decay at later times (regime II, for $t > 50 \,\mathrm{ps}$). By resolving the PL decay in both energy and time domains, we find that the weight of the total emission intensity dynamically shifts from short-lived bright X_0 excitons and negatively charged trions, X_1^- and X_2^- , (regime I) to longer lived excitonic species (regime II), as apparent in Fig. S6B. For delay times exceeding 50 ps after the pulsed excitation, more than 65% of all detected photons arise from D_0 , XX^- and D^- peaks. To avoid the effects of hot carrier transport and the subsequent cooling regime occurring within the first tens of ps⁶⁰, we focus our exciton propagation analysis in the main manuscript on delay times larger than 50 ps (regime II). Hence, the exciton diffusion coefficients determined in this time range primarily reflect the average propagation of dark D_0 excitons and their many-body excitonic complexes XX^- and D^- .

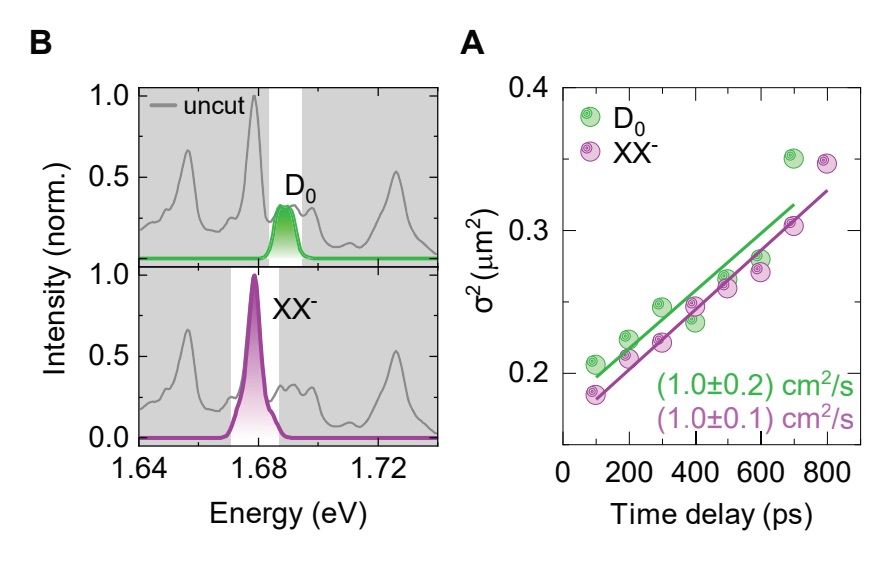
To confirm the hypothesis that the anisotropic transport in our hybrid 1D-2D structures is primarily carried by these excitons, we spectrally filtered the emission of each the D_0 and the XX^- excitons from the spectrum recorded in the strained region, before measuring their diffusion in time-resolved emission microscopy (see Fig. S7). For D_0 excitons propagating along the longitudinal axis, we find a diffusion coefficient of $D_x^{D_0} = (1.0 \pm 0.2) \, \mathrm{cm}^2/\mathrm{s}$ and analogously determine a diffusion coefficient of $D_x^{XX^-} = (1.0 \pm 0.2) \, \mathrm{cm}^2/\mathrm{s}$ for XX^- excitons. These values derived from the isolated emission of D_0 and XX^- compare reasonably well with the diffusion coefficient, $D_x = (1.4 \pm 0.1) \, \mathrm{cm}^2/\mathrm{s}$, we obtain when spectrally averaging the emission of all peaks.

8. DENSITY-DEPENDENT MEASUREMENTS

We investigate the robustness of the anisotropic exciton transport in our hybrid 1D-2D structure by monitoring the exciton propagation in the longitudinal x- and the transverse y-direction for different exciton densities. The exciton density n_X is calculated from the incident photon flux using



SUPPLEMENTARY FIGURE S6. Exciton decay dynamics at 4K. (A) Spectrally and spatially integrated PL transients recorded in strained and unstrained regions of the sample. The transients are essentially identical for the two regions, both featuring a fast initial decay and a slower decay in the regime, where the diffusion measurements are analyzed. (B) Spectrally resolved PL emission recorded in a strained region integrated from 0 ps to 50 ps (yellow) and from 50 ps to 1100 ps (blue) recorded in a strained region. Measurements were conducted under $5 \,\mu\text{J/cm}^2$ energy density per pulse of 1.77 eV excitation.

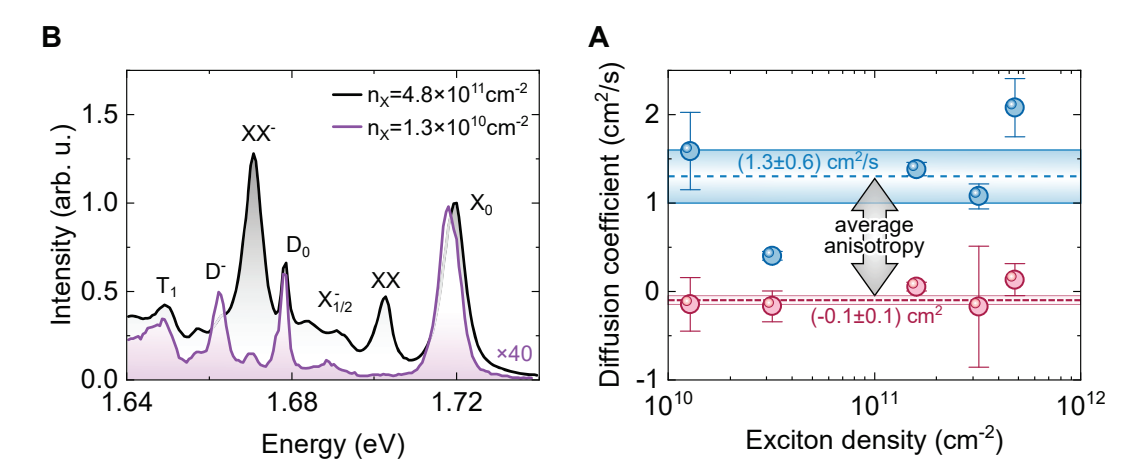


SUPPLEMENTARY FIGURE S7. Spectrally isolated diffusion of D_0 and XX^- at T=4 K. (A) Prior to recording the (spectrally integrated) exciton propagation in time-resolved emission microscopy measurements, the PL emission obtained in the strained region was dispersed in a spectrometer to select a narrow spectral window by a combination of two tunable edge pass filters, indicated by the grey shaded areas. The upper and lower panel shows their selective transmission centered around the emission peak of D_0 excitons and charged XX^- biexcitons, respectively. The grey spectrum in the background represents the PL spectrum obtained without the two tunable filters. (B) A linear fit to the transient broadening of the emission profiles along the longitudinal x-direction determines a diffusion coefficient for D_0 and XX^- individually. Measurements were conducted under $5 \mu J/cm^2$ energy density per pulse of $1.77 \, eV$ excitation.

$$n_{\rm X} = \frac{\bar{P}}{h\nu} f_{rep}^{-1} \alpha(h\nu). \tag{S4}$$

Here, \bar{P} is the time-averaged power density of the focused excitation laser and $f_{rep}=80\,\mathrm{MHz}$ is the repetition frequency of the laser pulses. From the linear reflectance measurements shown in Section 3, we find an absorption $\alpha(h\nu)$ of 0.8% for an excitation energy of $h\nu=1.77\,\mathrm{eV}$. Evaluating Eq. (S4) under the conditions indicated above results in an optically excited exciton density ranging from $n_{\mathrm{X}}=1.3\times10^{10}\mathrm{cm}^{-2}$ to $n_{\mathrm{X}}=4.8\times10^{11}\mathrm{cm}^{-2}$ in our experiments.

The two PL spectra obtained for the lowest and highest exciton density shown in Fig. S8A demonstrate a strongly non-linear dependence of the WSe₂ emission spectra under increasing excitation power. In our time and spatially resolved emission microscopy measurements, such substantial changes in the PL spectra directly imply a different excitonic composition of the spectrally integrated signals. Hence, different excitonic species contribute to the average



SUPPLEMENTARY FIGURE S8. Density dependent anisotropic exciton transport at T=4 K. (A) Time-integrated μ -PL emission spectra recorded in the strained region for two different exciton densities corresponding to the lowest and highest exciton density in (B). The spectrum at lower excitation density (purple) was multiplied by a factor of 40 to increase visibility. (B) Exciton density dependence of diffusion coefficients determined along the longitudinal x- and the transverse y-direction of the hybrid 1D-2D structure discussed in the main manuscript. At all densities, the exciton transport is highly anisotropic. Average diffusion coefficients in the longitudinal x- and transverse y-direction are (1.3 ± 0.6) cm²/s and (-0.1 ± 0.1) cm²/s, respectively. Numbers in brackets denote the average value and the corresponding standard deviation.

diffusion coefficient extracted for each excitation density. Nonetheless, we find strongly anisotropic propagation at all exciton densities, as illustrated in Fig. S8B, demonstrating the robustness of anisotropic exciton transport in hybrid 1D/2D structures. This observation is a direct consequence of the universal impact of strain on the exciton energy, which creates a potential minimum for all excitonic species, as shown in Fig. S1.

9. ESTIMATED OCCUPATION OF TRANSVERSE EXCITON MODES IN STRAIN-INDUCED CONFINEMENT CHANNELS

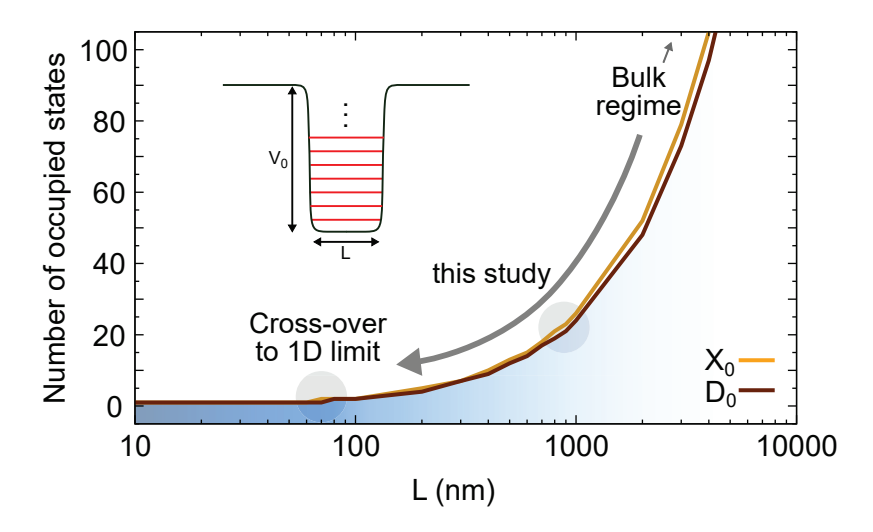
In order to estimate the number of exciton states (quantized transverse modes) confined in strained channels, we neglect the complex multi-valley band structure giving rise to a manifold of excitonic species and instead evaluate only for X_0 and D_0 excitons the exciton center-of-mass motion in the presence of a confinement potential exemplary. The exciton levels are quantized in the direction perpendicular to the confinement potential channel whereas the energy dispersion as function of the momentum along the channel is not affected. The Hamiltonian in the confined direction can be written as

$$H(y) = \frac{\hbar^2}{2M} \frac{\partial^2}{\partial y^2} + V(y), \qquad (S5)$$

in which $M=m_c+m_v$ is the exciton center-of-mass, $m_{c(v)}$ is the effective mass of the conduction (valence) band, V(y) is the confinement potential and y is the transverse direction of the hybrid 1D-2D structure (cf. Fig. 1B in the main text). We emphasize that this approach is valid as long as the exciton radius is smaller than the spatial scale of the confinement potential we are considering^{61,62}. Particularly, excitons in WSe₂ have a radius of 1-2 nm^{57,63-65} and therefore our analysis remains valid if we restrict ourselves to length scales > 10 nm, which is satisfied by the current setup of $\sim 1 \ \mu \text{m}$ (cf. Fig. 1B).

Using the electron and hole effective masses provided in Ref.⁵⁴, we obtain $M = 0.75m_0$ for D_0 and $M = 0.64m_0$ for X_0 , where m_0 is the free electron mass. For the confinement potential, we consider a finite square well with barrier height $V_0 = 10 \,\text{meV}$ and width L.

In Fig. S9 we show the number of confined states, which are populated by excitons with a thermal excitation energy below 0.35 meV (= k_BT at 4 K). For a potential width of 1 μ m (similar to our experiments) only \sim 25 of the emergent quantized transverse exciton modes are populated. Given that confined excitons in our experiment still scatter frequently between different transverse modes (mode spacing $\ll k_BT$), the quasi-1D channels are ascribed to the transverse diffusive regime, opposed to transverse ballistic 1D systems. Decreasing the spatial scale of the confinement potential, we estimated a cross-over to the true 1D regime (in which a single-mode is populated) to



SUPPLEMENTARY FIGURE S9. Estimated number of quantized modes populated by excitons. For the values of L shown in the plot, the results are nearly identical if a barrier height of $V_0 = 5$ meV is considered or even if we consider the infinite square well limit $V_0 \to \infty$.

occur at 60-70 nm, which is still large enough to consider the center-of-mass description of the excitons presented here.

10. ANISOTROPIC EXCITON TRANSPORT AND POSITION-DEPENDENT SCATTERING AT ROOM-TEMPERATURE

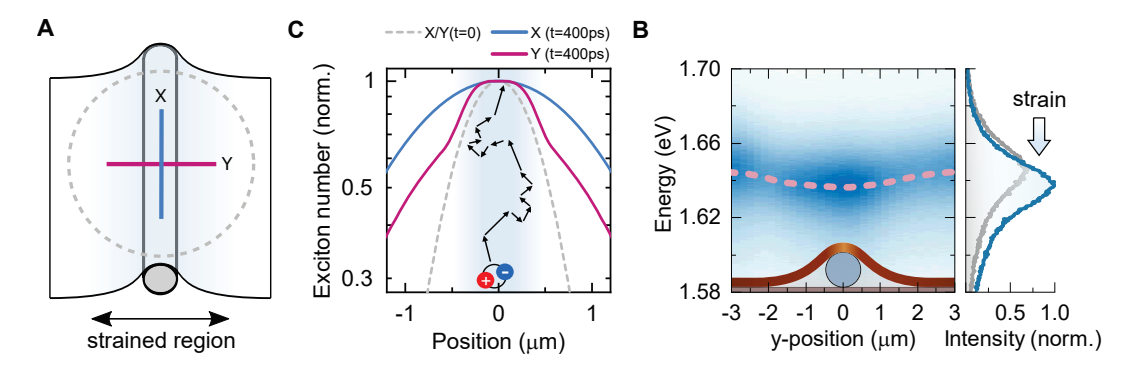
Here we propose a modification to the exciton transport model, going beyond confinement-induced effects, to rationalize the experimentally observed strong anisotropy of exciton transport in hybrid 1D/2D structures at room temperature. However, we also note that due to complex exciton-phonon interactions in the multi-valley band-structure^{25,26,31,32}, exciton density-dependent Auger effects and the subtle equilibrium dynamics between excitons and the electron-hole plasma state³⁸, a quantitative transport description of excitons in TMDCs at room temperature requires considerations beyond the simplified picture of linear diffusion of a single exciton species.

Firstly, analogous to low temperatures, tensile strain creates a confinement potential $u=u(\mathbf{r})$ with a depth of $10\,\mathrm{meV}$, which – while no longer fully suppressing the exciton transport – still significantly reduces the propagation of excitons in the y-direction (see discussion below). Secondly, local strain in WSe₂ causes a position-dependent exciton scattering rate at room temperature (evidenced in Fig. 4 of the main manuscript), equivalent to a spatially dependent diffusivity of excitons. This scattering rate determined from PL emission stems only from bright X_0 excitons, whereas the diffusion observed in our time-resolved emission microscopy experiments reflects the scattering of excitons populating different valleys. Indeed, this composite diffusion coefficient primarily contains contributions from excitons in spin and momentum-forbidden dark states, in addition to a significant contribution from the electron-hole plasma state³⁸. As a result, a realistic assessment of the strain-dependent exciton scattering rate required to quantitatively simulate our experiment is not straightforward.

Here, to demonstrate the general effect of position-dependent scattering on the propagation of excitons in WSe₂, we simulate Eq. (S6) based on a conservative estimate: a moderate increase of the diffusion coefficient from $D_{unstrained} = 9 \text{ cm}^2/\text{s}$ to $D_{strained} = 12 \text{ cm}^2/\text{s}$ is extracted from the calculations presented in Ref.³² for excitons in non-encapsulated 1L WSe₂. We thus replace the previously constant D by a spatially dependent $D = D(\mathbf{r})$, which increases towards the center of the super-Gaussian strain profile in the y-direction, resulting in additional terms of the drift-diffusion model in Eq. (1) of the main manuscript:

$$\frac{\partial n}{\partial t} = D\Delta n + \nabla D \cdot \nabla n + \frac{D}{k_b T} \nabla n \cdot \nabla u + n \nabla u \cdot \nabla \frac{D}{k_b T} + \frac{D}{k_b T} n \Delta u - \frac{n}{\tau}.$$
 (S6)

We numerically calculate the time evolution of an initial Gaussian exciton density, $n(\mathbf{r}, 0) = n_0 \exp(-\mathbf{r}^2/2\sigma_0^2)$ with $\sigma_0 = 0.43 \,\mu\text{m}$, a temperature of $T = 300 \,\text{K}$ and an exciton decay time of $\tau = 40 \,\text{ps}$ and analyse the fraction of excitons residing within the initially excited area of the strained region (cf. sketch in Fig. S10A). From the



SUPPLEMENTARY FIGURE S10. Localization effect under the impact of position-dependent scattering at T = 290 K. (A) Schematic of the extracted exciton profiles along x and y. (B) Simulated exciton distribution profiles along x and y at 400 ps after the structure is excited with a symmetric Gaussian beam (grey dashed lines, t = 0 ps). Shaded area indicates the extension of the strained channel. (C) A μ -PL line scan of the exciton energy is accompanied by a 1.5-fold increase of the integrated emission intensity in the center of the strain. The dashed line traces the energy-dependence of the emission peak along the y-direction. PL spectra were recorded in an unstrained ($y = 3 \mu \text{m}$, grey) and strained ($y = 0 \mu \text{m}$, blue) region of the vdW stack.

data plotted in Fig. S10B, we find that after 400 ps less than 40% of the excitons are found in the initially excited area in the x-direction. Along y, however, approximately 90% of the carriers injected into the strained region are still localized in this part of the structure, even after 400 ps. In this case, the degree of anisotropy of exciton localization amounts to $\sim 40\%$, indicating a substantial direction-dependent exciton localization effect in our hybrid 1D/2D structure, which results in a strongly anisotropic transport of excitons. Note that if we remove the spatially dependent scattering from Eq. (S6), considering only the effects of the confinement potential on the transport of excitons with $D=9\,\mathrm{cm}^2/\mathrm{s}$ at room temperature, we still observe a significant anisotropy in the transport of excitons, which is, however, characterized by a reduced degree of only 20%. Despite the conservative estimate of the position-dependent diffusion coefficient, we thus find a strong impact of strain on the room-temperature diffusion observed in our experiments.

In addition, Fig. S10C demonstrates a 1.5-fold increase of the integrated emission intensity in the strained region, qualitatively similar to the observations in a recent study on homogeneously strained WSe_2^{26} . In our structure, such a local enhancement in the PL emission intensity along the y-direction is consistent with the interpretation of funneling and the observed propagation.

^{*} These authors contributed equally.

[†] alexey.chernikov@tu-dresden.de

[†] menon@ccny.cuny.edu